A&A, 701, A197 (2025)
https://doi.org/10.1051/0004-6361/202452951

Astronomy & Astrophysics

Visible-light channel of the Metis/Solar Orbiter coronagraph: On-ground polarimetric calibration

M. Casti[1,⋆], S. Fineschi[1], G. Capobianco[1], A. Liberatore[1], M. Romoli[2,3], E. Antonucci[1], A. Álvarez-Herrero[4], V. Andretta[5], V. Da Deppo[6,5], F. Frassetto[6], C. Grimani[7,8], P. Heinzel[9,10], F. Landini[1], D. Moses[11], G. Massone[1], G. Naletto[12], G. Nicolini[1], M. Pancrazzi[1], P. García Parejo[4], D. Spadaro[13], M. Stangalini[14], R. Susino[1], L. Teriaca[15], and M. Uslenghi[16]

[1] INAF, Astrophysical Observatory of Torino, Via Osservatorio 20, Pino Torinese (TO), I-10025, Italy
[2] INAF, Arcetri Astrophysical Observatory, Largo Enrico Fermi 5, I-50125 Florence, Italy
[3] Department of Physics and Astronomy, University of Florence, Via Giovanni Sansone 1, Sesto Fiorentino (FI), I-50019, Italy
[4] Instituto Nacional de Técnica Aeroespacial, Torrejón de Ardoz, Madrid S-28850, Spain
[5] INAF, Astronomical Observatory of Capodimonte, Salita Moiariello 16, Napoli I-80131, Italy
[6] CNR – Institute for Photonics and Nanotechnologies, Via Trasea 7, I-35131 Padua, Italy
[7] Dip. di Scienze Pure e Applicate, Università di Urbino, Via Santa Chiara, 27, 61029 Urbino, Italy
[8] INFN Sezione di Firenze, Via B. Rossi 1, 50019 Sesto Fiorentino, Florence, Italy
[9] Academy of Science of the Czech Republic Fričova 298, 251 65 Ondřejov, Czech Republic
[10] University of Wroclaw, Center of Scientific Excellence – Solar and Stellar Activity, Kopernika 11, 51-622 Wroclaw, Poland
[11] NASA Headquarters, Washington DC 20546-0001, USA
[12] Department of Physics and Astronomy, University of Padua, Via Francesco Marzolo 8, Padova I-35131, Italy
[13] INAF, Astrophysical Observatory of Catania, Via Santa Sofia 78, Catania I-95123, Italy
[14] ASI, Via del Politecnico, 00133 Roma, Italy
[15] Max-Planck-Institut für Sonnensystemforschung, Justus-von-Liebig-Weg 3, D-37077 Göttingen, Germany
[16] INAF, Istituto di Astrofisica Spaziale e Fisica Cosmica, Via Alfonso Corti 12, I-20133 Milan, Italy

Received 11 November 2024 / Accepted 7 July 2025

ABSTRACT

Context. Metis is the solar coronagraph on board the ESA/NASA mission Solar Orbiter (SolO), launched in 2020. It is designed to acquire simultaneous images of the solar corona in visible polarized light (580–640 nm), and in the narrowband H I Lyman-α line (i.e., 121.6 nm). The instrument visible-light channel includes a polarimeter composed of two liquid crystal variable retarder (LCVR) cells, a quarter-wave plate, and a linear polarizer, with the LCVR cells acting as the modulating element. By applying a specific voltage to the cells, it is possible to modify the incoming polarized light by changing the direction of the associated vector by a known angle, i.e., the angle of retardance.
Aims. The polarimetric characterization of Metis is needed to correctly derive the properties of the plasma in the observed solar corona. This work describes the steps we took to fully characterize the visible channel of the Metis coronagraph, i.e., by deriving the modulation and demodulation matrices for each pixel, the latter being the key element for deriving the Stokes vector of the observed K corona. We completed the characterization by deriving the error associated with the derived values.
Methods. The first step is to fully characterize the Metis polarimeter. This is needed to derive the relation between the voltage applied to the liquid crystal cells and the angle of retardance imposed on the incoming polarized light. This step represents the starting point for the calibration of the full instrument.
Results. We derived (i) the voltage versus retardance curve associated with the polarimeter and (ii) the demodulation tensor of the Metis coronagraph, which is now used to retrieve the Stokes vector that describes the coronal light polarization state.
Conclusions. This calibration is fundamental to disentangle the coronal light from the instrumental effects, such as disuniformity and instrumental polarization.

Key words. instrumentation: polarimeters – methods: data analysis – space vehicles: instruments – techniques: polarimetric – telescopes – Sun: corona

1. Introduction

Solar Orbiter (SolO) (Marsch et al. 2000; Müller et al. 2020) is a heliospheric space mission. It is a product of the international cooperation between the European Space Agency (ESA) and the US National Aeronautics and Space Administration (NASA). The satellite was launched in February 2020, and the nominal five-year mission began in November 2021. Its primary goal is to explore the innermost accessible region of the solar corona to provide new insight into how the Sun creates and controls the heliosphere, how the solar wind originates, and how it evolves near the Sun. The mission profile encompasses flying on a highly elliptic orbit, between 0.9 AU at aphelion and 0.28 AU at perihelion, with a progressively increasing angle of inclination with respect to the ecliptic plane up to 30 deg at the end of the extended mission. This will provide an unprecedented point of

⋆ Corresponding author: marta.casti@inaf.it

view on the poles of the Sun for the remote sensing instruments on board the satellite. The SolO scientific payload consists of ten complementary instruments, both remote sensing and in situ. This suite of instruments is capable of providing a unique combination of measurements. Since the beginning of the mission, Solar Orbiter provided new insights into the phenomena taking place and observed in the solar corona. Several papers in the literature testify to the new outstanding results of this mission (Romoli et al. 2021; Berghmans et al. 2021; Telloni et al. 2022, 2023; Antonucci et al. 2023).

Metis (Antonucci et al. 2020; Fineschi et al. 2020) is the solar coronagraph on board Solar Orbiter. It is uniquely capable of acquiring simultaneous full images of the solar corona projection on the plane of the sky in two different wavelength ranges, one in the visible and one in the UV portion of the spectrum. These dual observations are achieved thanks to a filter placed in its optical path that separates these two spectral components of the incident light by reflecting the visible one and transmitting the UV. While the wavelength range of the former is broad and goes from 580 to 640 nm, that of the latter is very narrow and is dedicated to capturing the emissions of the hydrogen Lyman-α with a central wavelength at 121.6 nm (Antonucci et al. 2000, 2012; Naletto et al. 2010; Fineschi et al. 2013) and extending about 10 nm. This dual-channel design extends that of the UltraViolet Coronagraph Spectrometer (UVCS; Kohl et al. 1995) on board the Solar and Heliospheric Observatory mission (SOHO; Domingo et al. 1995), providing the ability to acquire full images. The Solar CORonograph Experiment (SCORE; Fineschi et al. 2003; Landini et al. 2006), the solar coronagraph for the suborbital mission *Herschel* (Moses et al. 2020), which was conceived as a prototype for the Metis coronagraph, is also based on this same UVCS heritage.

Within its visible-light optical path, Metis is provided with a polarimeter that allows the observation of the polarized continuum component of the solar corona. These measurements are an important element for characterizing the plasma that constitutes the atmosphere of the Sun. The continuum component of the coronal spectrum, the K corona, originates from Thomson scattering: the photospheric radiation is scattered by the free electrons located in the coronal medium. Due to the consequent vibration of the electrons, this process originates polarized light, whose intensity is directly related to the presence of electrons (Billings 1966). Consequently, from measurements of the K coronal polarized brightness, it is possible to derive the density of the electrons in the Sun's atmosphere as a function of the radial distance from the center of the Sun (Minnaert 1930; Van de Hulst 1950). Observing the solar corona in polarized light is advantageous because it permits one to exclude the contribution of the F corona, which is originated by the scattering of the radiation by interplanetary dust particles and therefore does not provide any information on the status of the electrons. The F corona is assumed to be unpolarized for heliocentric heights lower than 8 solar radii ($R_\odot$), while at higher altitudes its polarization is no longer negligible (Koutchmy & Lamy 1984, 1985; Mann 1992; Lamy et al. 2020, 2021). The evaluation of the electron density in the corona derived using the brightness, without a proper removal of the contribution of the F corona, could result in an overestimation of the presence of electrons. Electron density measurements play a fundamental role in our understanding of the physics of the solar corona; the total radiative losses from the corona depend on the square of the electron density, and this is connected to the coronal energetics and to the heating input required for the corona to exist. Another advantage of acquiring observations in polarized light is the possibility of increasing the signal-to-noise ratio in the data by eliminating the instrumental spurious light, i.e., stray light composed of the diffraction generated by the coronagraph occulting element and then scattered by the optics. The simultaneous observation of the solar corona in polarized visible light and in the Ly-α line provides a direct measurement of the proton outflow velocity in the acceleration region. These measurements are necessary to connect the solar wind to its source region on the Sun, and they would be otherwise impossible at heliocentric altitudes lower than 9 solar radii. The method used to derive these measurements is based on the Doppler dimming effect, which is observable in the intensities and profiles of UV and extreme-UV spectral lines whose emission is due to the resonant scattering of chromospheric light, such as Ly-α (Hyder & Lites 1970). The so-called Doppler dimming technique is explained in detail by Withbroe et al. (1982), and it has previously been applied to SOHO/UVCS data, leading to breakthrough results (Kohl et al. 1997; Cranmer et al. 1999; Antonucci et al. 2000; Cranmer 2020).

The techniques developed to measure the polarization state of the observed signal are based on the modulation of the intensity of the incident radiation. This can be done in the temporal, spatial, or spectral domain (Tyo et al. 2006; Snik et al. 2014). Metis measures the polarized brightness of the solar corona by acquiring a set of images in each of which the initial polarization state of the coronal light has been altered by a known amount; it thus implements a temporal modulation of the incident light. This modulation is accomplished through the use of a polarimeter, which is composed of three elements: a quarter-wave plate, two liquid crystal variable retarder (LCVR) cells forming the polarization modulation package (PMP), and a linear polarizer (LP). In this composition, the PMP is the electro-optical modulating element. The two LCVR cells, which contain nematic liquid crystals, can in fact change their birefringence in the presence of an electric field, acting locally as a uniaxial retardation plate (Saleh & Teich 1991; Uribe-Patarroyo et al. 2011).

This paper describes the setup and the procedure implemented to acquire the data within the framework of the on-ground calibration activities of the Metis polarimetric visible-light channel. We present the analysis of the collected dataset and the obtained results, and explain their relevance. The first step of the procedure is the full characterization of the polarimeter, before its integration into the instrument. The results we obtained are fundamental to comprehending how the polarimeter works as a single element and allowed us to disentangle the effects of the polarimeter itself from the instrumental polarization. Once the Metis coronagraph was fully integrated, the goal of the calibration activities was to understand whether and how the incident polarized light is modified by the instrument, not only by the known amount resulting from the polarimeter activation but also by the other components of the instrument. It is well known that every element in an instrument's optical path can be the source of an unwanted alteration in the polarization of the observed signal (Chipman 1988, 1990; McGuire & Chipman 1994).

The outcomes of this work are threefold: (i) the mathematical relationship linking the applied voltage to the angle of rotation induced by the cells on the polarization vector of the incoming light; (ii) a set of two-dimensional arrays collecting the element of the demodulation matrix associated with each pixel of the Metis coronagraph, and (iii) the related uncertainties.

Section 2 provides a brief description of the Metis coronagraph and its polarimeter, detailing the mathematical model used to describe how the polarized incident light is modified before reaching the detector. Section 3 gives an overview of

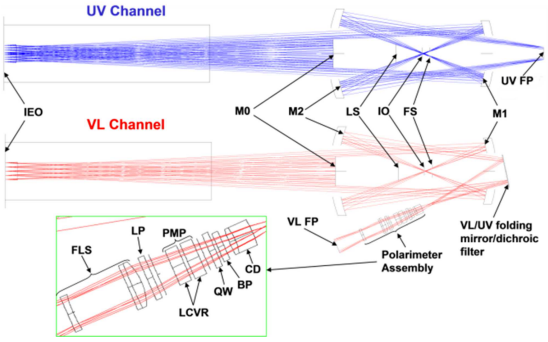

Fig. 1. Metis coronagraph ray trace. The UV and the visible-light channels are depicted separately for visualization purposes, but the two components follow the same path until the dichroic filter. The solar light enters the instrument through the inverted external occulter (IEO), and the Sun disk light is reflected by the M0 mirror out of the instrument. A primary (M1) and a secondary (M2) mirror collect the coronal light together with the light diffracted by the IEO and M0. This second component is blocked thanks to the presence of the internal occulter (IO) and the Lyot stop (LS). Finally, the coronal light is split into the two observational components by the dichroic filter and directed toward the respective detectors. Before reaching the detector, the visible-light component passes through the polarimeter assembly, here shown broken down into its optical elements.

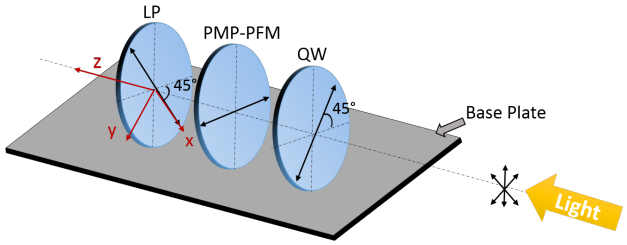

Fig. 2. Schema of the Metis polarimeter. It is composed of a QW, the PMP with two LCVR cells, and a LP in the DeSenarmont configuration.

the calibration of the Metis polarimeter and outlines the use of the generic mathematical model applied to the specific case of the Metis coronagraph to characterize the instrument response. Section 4 provides a summary of the conclusions, highlighting key findings and implications.

2. The Metis coronagraph and the polarimeter

The development of the Metis coronagraph is the result of an international collaboration led by the National Institute for Astrophysics (INAF), Astrophysics Observatory of Turin (OATo), Italy.

2.1. The Metis polarimeter

One of the unique features of the Metis coronagraph is its capability to simultaneously observe the solar corona within two different wavelength ranges. This is possible due to the presence of two different optical channels within the instrument, as shown in Fig. 1. A detailed description of the Metis design can be found in the literature (Antonucci et al. 2020; Fineschi et al. 2020); therefore, it is here omitted.

The Metis polarimeter assembly (Fineschi et al. 2005; Crescenzio et al. 2012) is located within the visible-light path of the instrument (see Fig. 1). It is composed of a bandpass filter, a fixed achromatic quarter-wave retarder (QW), the PMP, and a LP. The bandpass filter is needed to isolate the wavelength range of interest, from 580 to 640 nm, while the QW and the LP comprise the DeSenarmont configuration (De Senarmont 1840; Bass 1995) adopted in the polarimeter design. Figure 2 is a schematic of the Metis polarimeter showing the orientation of the maximum transmission axis for each of its elements.

The modulation of the incident polarized light performed by the Metis polarimeter is achieved by applying a voltage to the two LCVR cells that comprise the PMP. These cells contain liquid crystals, which are molecules in an intermediate matter state between ordinary liquids and three-dimensional solids. The resulting optical element contains an anisotropic medium that acts locally as a uniaxial retardation plate and exhibits optical birefringence (Saleh & Teich 1991). The operating principle is the following: a voltage is externally applied to the cell to create an electric field around the liquid crystal molecules, which react by changing their position within the cell to adapt to the new environment. The consequence of this new orientation of the molecules inside the cells is a change in the intrinsic properties of the material that results in the ability to modify the state of polarization of the refracted light. The relationship between the effect of the cells on the polarization state of the incident light and the applied voltage is not linear, and it changes for different operational temperatures of the cells. The LCVR cells are made of two 5 mm glasses coated on one side with a transparent conductive material, indium tin oxide (ITO), and an alignment layer (rubbed polyimide), while on the other side there is an antireflective coating. The cells are oriented with their fast axes parallel with respect to each other but with the pretilt angles of the liquid crystal molecules in opposite direction. A detailed description is given in Álvarez Herrero et al. (2015) and García Parejo & Álvarez-Herrero (2019), while the manufacturing process is detailed in Alvarez-Herrero et al. (2017).

The advantages of using liquid crystals for polarimetric measurements have been highlighted in different previous works (Heredero et al. 2007; Alvarez-Herrero et al. 2011, 2024). It is worth mentioning that there are some downsides related to the optical performance of liquid crystal retarders, and some of these are mitigated in the Metis by design. Their ability to modify the polarization state of the incident light of a known angle is directly related to the orientation of the enclosed molecules. As a consequence, different rays travel along different paths and encounter different molecules when they pass through the cells. Therefore, it is necessary to characterize their effect on the incident polarized light across the entire field of view. Furthermore, because the LCVR devices rely on the position of the molecules to modulate light, they are sensitive to temperature to some degree. To mitigate this effect, the Metis polarimeter has been provided with a temperature controller, which guarantees a uniform and stable temperature of the liquid crystal inside the cells (Silva-López et al. 2017). Finally, the retardance angle applied to the incoming light is also dependent on the angle of incidence with which the light encounter the cells. This is the reason why the liquid crystal molecules inside the LCVR cells composing the Metis PMP are displaced with an opposite tilt angle of ±7° (see Fig. 3), which ensures a wider field of view angle to the polarimeter (Capobianco et al. 2018; Parejo et al. 2019).

2.2. Mathematical model

The Metis polarimeter can be mathematically described using the Mueller calculus (Collett 1992), which is suitable to describe the polarimetric effects of an optical element on the incident light

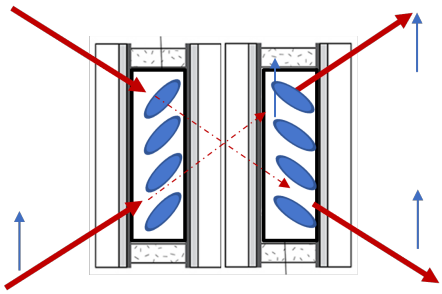

Fig. 3. Schema of the Metis PMP. The Metis PMP is composed of two identical LCVR cells with the same orientation, but the pre-tilt angles of their molecules are in opposite directions to increase their acceptance angle.

beam. The Mueller calculus links the polarization state of the incident light to the one of the signal exiting the optical element by means of a linear system of four equations:

$$\boldsymbol{S}_{\rm out} = \begin{bmatrix} I \\ Q \\ U \\ V \end{bmatrix}_{\rm OUT} = \begin{bmatrix} m_{00} & m_{01} & m_{02} & m_{03} \\ m_{10} & m_{11} & m_{12} & m_{13} \\ m_{20} & m_{21} & m_{22} & m_{23} \\ m_{30} & m_{31} & m_{32} & m_{33} \end{bmatrix} \cdot \begin{bmatrix} I \\ Q \\ U \\ V \end{bmatrix}_{\rm IN} = M \cdot \boldsymbol{S}_{\rm in}. \quad (1)$$

Here, $\boldsymbol{S} = (I, Q, U, V)$ is the so-called Stokes vector, which describes the polarization state of light, and M is the Mueller matrix that describes the polarization-altering characteristics of the optical element. I, Q, U, and V are measurable quantities that represent four physically independent features of the polarized radiation; intensity (I), linear (Q, U), and circular (V) polarization.

In the Mueller calculus, the Mueller matrix associated with systems composed of several polarimetric elements is simply given by the result of the multiplication of the matrices describing its elements. To build the mathematical model, we started with the theoretical Mueller matrix associated with the main polarization elements, such as LPs and retarders, which can be easily found in the literature (Collett 2005).

The crystals inside the LCVR cells act as a uniaxial retardation plate, with an angle of retardance, δ, introduced in the incident polarized light depending on the applied voltage. Therefore, one can use the Mueller matrix associated with an ideal quarter-wave plate to mathematically describe the LCVR cells within the Metis polarimeter, where the angle δ is a function of voltage. The Mueller matrix associated with the Metis polarimeter is obtained from the theoretical Mueller matrix of its components after combining them as per the following equation:

$$\begin{aligned} M_{\rm POL_{th}} &= M_{\rm LP} M_{\rm LCVR_1}(\delta(V)) M_{\rm LCVR_2}(\delta(V)) M_{\rm QW} \\ &= M_{\rm LP} M_{\rm PMP}(\delta_{\rm PMP}(V)) M_{\rm QW}. \end{aligned} \quad (2)$$

We considered a reference frame where: the Z-axis is in the light propagation direction; the X-axis is parallel to the LP acceptance axis; and the Y-axis completes the right-handed set; the fast axis of the LCVR cells are therefore at −45° from the LP acceptance axis; and the fast axis of the QW is at 90° (see Fig. 2).

Because of the strict requirements assigned for the integration of the polarimeter optics and on the basis of the measurements performed during their integration, the analysis considers the quarter wave fast axis and the LP acceptance axis positioned as designed, with a positioning error within the tolerances. Moreover, based on the results obtained during the calibration of these optical elements, we consider them ideal. The average value of retardation measured for the QW plate within the Metis bandpass is in fact equal to 90.4°. When the difference of 0.4° from the ideal case is used to derive its effect on the measured intensity downstream of the polarimeter, the result yields a circular polarization component of approximately 2.4e−5, which is negligible according to Crescenzio et al. (2012).

The resulting Mueller matrices associated with the three optical elements that comprise the polarimeter are reported in the following equations:

$$M_{\rm LP}(\theta = 0) = \frac{1}{2} \begin{bmatrix} 1 & 1 & 0 & 0 \\ 1 & 1 & 0 & 0 \\ 0 & 0 & 0 & 0 \\ 0 & 0 & 0 & 0 \end{bmatrix} \quad (3)$$

$$M_{\rm PMP}\left(\theta = -\frac{\pi}{4}, \delta(V)\right) = \begin{bmatrix} 1 & 0 & 0 & 0 \\ 0 & \cos(\delta_{\rm PMP}(V)) & 0 & -\sin(\delta_{\rm PMP}(V)) \\ 0 & 0 & 1 & 0 \\ 0 & \sin(\delta_{\rm PMP}(V)) & 0 & \cos(\delta_{\rm PMP}(V)) \end{bmatrix} \quad (4)$$

$$M_{\rm QW}\left(\theta = \frac{\pi}{2}\right) = \begin{bmatrix} 1 & 0 & 0 & 0 \\ 0 & 1 & 0 & 0 \\ 0 & 0 & 0 & 1 \\ 0 & 0 & -1 & 0 \end{bmatrix}. \quad (5)$$

Equation (4) is the result of the combination of the two LCVR cells; therefore, the δ angle corresponds to their combined effect: $\delta_{\rm PMP} = \delta_{\rm LCVR_1} + \delta_{\rm LCVR_2} \equiv \delta$. By multiplying these matrices as shown in Eq. (2), it is possible to retrieve the Mueller matrix that describes the entire Metis polarimeter:

$$M_{\rm POL} = \frac{1}{2} \begin{bmatrix} 1 & \cos(\delta(V)) & \sin(\delta(V)) & 0 \\ 1 & \cos(\delta(V)) & \sin(\delta(V)) & 0 \\ 0 & 0 & 0 & 0 \\ 0 & 0 & 0 & 0 \end{bmatrix}. \quad (6)$$

This matrix describes how the Metis polarimeter can change the polarimetric characteristics of the light beam that passes through it. From this equation, we notice two main aspects: (i) the effect of the polarimeter on the incoming light depends on the voltage applied to the cells containing the liquid crystals, (ii) since the last row and the last column of the matrix are composed of zeros, this configuration does not modulate the circularly polarized radiation, $m_{03} = 0$. It is worth to point out that in this formulation of the Mueller matrix associated with the Metis polarimeter the displacement error of the optics is known and negligible and the transmissivity of all the optical elements is considered maximum along their main axis and equal to zero along its perpendicular one. By combining Eqs. (1) and (6) it is possible to see how, in the model, the intensity of the light measured downstream the polarimeter depends on the voltage:

$$\begin{aligned} I_{\rm OUT} &= m_{00} \cdot I_{\rm IN} + m_{01} \cdot Q_{\rm IN} + m_{02} \cdot U_{\rm IN} + m_{03} \cdot V_{\rm IN} \\ &= \frac{I_{\rm IN}}{2} + \frac{\cos(\delta(V))}{2} \cdot Q_{\rm IN} + \frac{\sin(\delta(V))}{2} \cdot U_{\rm IN}. \end{aligned} \quad (7)$$

3. Calibration of the Metis visible-light channel

The goal of polarimetrically calibrating the Metis visible-light channel was to understand the effect of the instrument on the observed polarized light. We need to know this to be able to measure the polarization state of the K corona and to remove the contribution of any polarization effects introduced by the instrument in the detected signal. The result of the calibration is a set of 12 matrices that, opportunely combined with the polarized

images acquired by the instrument, allows one to measure the Stokes vector describing the observed coronal signal and hence to derive the density of the electrons in the Sun atmosphere.

3.1. Mathematical model

The formulation of the mathematical model used to derive the polarimetric properties of the instrument is based on the Mueller calculus shown in Eq. (1). Since the polarization state of the observed signal cannot be directly measured by the telescope, the full Stokes vector has to be inferred from the acquired images, which contain the information related to the intensity of the light. This quantity corresponds to the first element of the output Stokes vector, $I_{\rm OUT}$, which is a function of the polarization state of the incident light (see Eq. (7)). As a consequence, the polarization of the observed solar corona can be measured by acquiring a set of at least three images, since the K corona is linearly polarized, and solving a new system of equations composed of these measurements. The set of measurements is acquired by changing the polarization state of the incident light of a known quantity, and this is achieved by means of a change in the optical characteristics of the instrument. Eq. (8) shows the system of equations that links the measurements acquired by changing the properties of the matter to the incident polarized light beam. The different acquisition conditions are indicated in the equation by the number in the apices. Each row of the X matrix in Eq. (8), the so-called modulation matrix, is composed of the elements of the first row of the Mueller matrix of the instrument under test:

$$\begin{bmatrix} I^{(0)} \\ I^{(1)} \\ I^{(2)} \\ I^{(3)} \end{bmatrix} = \begin{bmatrix} m_{00}^{(0)} & m_{01}^{(0)} & m_{02}^{(0)} & m_{03}^{(0)} \\ m_{00}^{(1)} & m_{01}^{(1)} & m_{02}^{(1)} & m_{03}^{(1)} \\ m_{00}^{(2)} & m_{01}^{(2)} & m_{02}^{(2)} & m_{03}^{(2)} \\ m_{00}^{(3)} & m_{01}^{(3)} & m_{02}^{(3)} & m_{03}^{(3)} \end{bmatrix} \cdot \begin{bmatrix} I \\ Q \\ U \\ V \end{bmatrix} = X \cdot \boldsymbol{S}. \tag{8}$$

The modulation matrix of the Metis polarimeter is reported in Eq. (9), where each row corresponds to a different voltage value and this is indicated by the number between brackets. As noted above, in our case study, the instrument is blind to the circular polarization and the elements of the last column and row are equal to zero:

$$X_{\rm Metis} = \frac{1}{2} \begin{bmatrix} 1 & \cos(\delta^{(0)}) & \sin(\delta^{(0)}) \\ 1 & \cos(\delta^{(1)}) & \sin(\delta^{(1)}) \\ 1 & \cos(\delta^{(2)}) & \sin(\delta^{(2)}) \\ 1 & \cos(\delta^{(3)}) & \sin(\delta^{(3)}) \end{bmatrix}. \tag{9}$$

By definition, the modulation matrix links the measured intensity with the observed polarized light, the latter being the unknown element. To derive a mean to evaluate the polarization state of the solar corona from the acquired measurements, we inverted the system shown in Eq. (8):

$$\boldsymbol{S} = \boldsymbol{X}^{\dagger} \cdot I_{\rm meas}. \tag{10}$$

The problem reduces to finding the inverse of the modulation matrix, the so-called demodulation matrix, $X^{\dagger}$, which can also be found as D in the literature. Since the modulation matrix is full column rank, it is necessary to make use of mathematical methods to derive the pseudo-inverse. In this analysis, we used the Monroe-Penrose method to obtain the inverted matrix.

$$\boldsymbol{X}^{\dagger} = \boldsymbol{D} = (\boldsymbol{X}^T \boldsymbol{X})^{-1} \boldsymbol{X}^T. \tag{11}$$

The strategy consists first in deriving the modulation matrix from data acquired in the laboratory, where we can introduce a light beam with a known Stokes vector into the instrument and then calculate its inverse. As a matter of fact, it is possible to rewrite Eq. (8) and derive four different systems of equations, one for each row of the modulation matrix, where the unknown parameters are the elements of the modulation matrix, and the matrix containing the known parameters is composed of the Stokes vectors of the light beams in input. Each of these systems of equations is then related to a raw of the modulation matrix. Eq. (12) shows how these systems of equations are composed:

$$\begin{bmatrix} I^{(0)} \\ I^{(1)} \\ \vdots \\ I^{(N)} \end{bmatrix} = \begin{bmatrix} I_{\rm IN}^{(0)} & Q_{\rm IN}^{(0)} & U_{\rm IN}^{(0)} \\ I_{\rm IN}^{(1)} & Q_{\rm IN}^{(1)} & U_{\rm IN}^{(1)} \\ \vdots & \vdots & \vdots \\ I_{\rm IN}^{(N)} & Q_{\rm IN}^{(N)} & U_{\rm IN}^{(N)} \end{bmatrix} \cdot \begin{bmatrix} m_{00}^{(i)} \\ m_{01}^{(i)} \\ m_{02}^{(i)} \end{bmatrix}. \tag{12}$$

Here i indicates the row number of the modulation matrix in Eq. (8), which, in the case of the Metis polarimeter, refers to a particular voltage. By solving three systems of equations composed as the one reported in Eq. (12), it is possible to derive all the elements of the modulation matrix. The hypothesis behind this strategy is that the element used in the laboratory to generate the set of known polarization states is capable of generating a perfectly polarized light beam. If this is verified, the Stokes vectors of the incoming beam will be equal to the theoretical ones. Finally, we want to point out that even if three different measurements of the incident light would be enough to determine its Stokes vector, we decided to over-constrain the system by acquiring four different measurements. The procedure described here to perform the polarimetric characterization of a telescope is not different from those applied in previous studies on other instruments and described in the literature, for example in Skumanich et al. (1997) and Capitani et al. (1989).

There are several possible combinations of voltage values that can be applied to the cells, and each will result in a different formulation of the modulation matrix. This aspect of the polarimetric characterization of an optical element via modulation and demodulation matrices has been addressed in the past (del Toro Iniesta & Collados 2000; Ramos & Collados 2008) resulting in the definition of a new parameter, which is the polarimetric efficiency. The higher the efficiency value, the closer the derived solution is to the optimum Stokes vector. The maximum efficiency vector for a complete Stokes polarimeter was found to be

$$\xi_i = \left(n \sum_{j=1}^{n} X_{ij}^{\dagger 2} \right)^{-\frac{1}{2}}, \tag{13}$$

where n is the number of measurements and i refers to the elements of the Stokes vector, with values from 1 to 4. In del Toro Iniesta & Collados (2000) it is demonstrated that the maximum obtainable polarimetric efficiency of the modulation scheme is

$$\xi_{\max,1} = 1; \sum_{i=2}^{4} \xi_{\max,i}^2 = 1. \tag{14}$$

If we consider voltage values that correspond to retardance angles equal to $\delta_0 = 0$, $\delta_1 = \frac{\pi}{2}$, $\delta_2 = \pi$, and $\delta_3 = \frac{3\pi}{2}$, the elements of the theoretical modulation matrix assume the following values,

$$X = \frac{1}{2} \begin{bmatrix} 1 & 1 & 0 \\ 1 & 0 & 1 \\ 1 & -1 & 0 \\ 1 & 0 & -1 \end{bmatrix}, \tag{15}$$

and, by inverting Eq. (15), the theoretical demodulation matrix becomes

$$X^{\dagger} = \frac{1}{2}\begin{bmatrix} 1 & 1 & 1 & 1 \\ 2 & 0 & -2 & 0 \\ 0 & 2 & 0 & -2 \end{bmatrix}. \tag{16}$$

The goal of the Metis polarimetric characterization is to obtain maximum polarimetric efficiency for the Stokes vector related to the linear polarization, Q and U. The efficiency vector is hence equal to

$$\epsilon_{\max} = \left(1, \frac{1}{\sqrt{2}}, \frac{1}{\sqrt{2}}\right). \tag{17}$$

To evaluate the error associated with the derived demodulation matrix, we started by evaluating the solution of the linear system of equations in the cases of maximum error. In other words, we solved again the system of equations shown in Eq. (12) for two different cases: replacing the measurements with (i) the sum of the measurement and its error, and (ii) the difference between the measurement and its associated error. The two resulting new systems of equations account for the highest possible error associated with the measurements:

$$\begin{bmatrix} I^{(0)} \\ I^{(1)} \\ \vdots \\ I^{(N)} \end{bmatrix} = \begin{bmatrix} I_{\rm IN}^{(0)} & Q_{\rm IN}^{(0)} & U_{\rm IN}^{(0)} \\ I_{\rm IN}^{(1)} & Q_{\rm IN}^{(1)} & U_{\rm IN}^{(1)} \\ \vdots & \vdots & \vdots \\ I_{\rm IN}^{(N)} & Q_{\rm IN}^{(N)} & U_{\rm IN}^{(N)} \end{bmatrix} \cdot \begin{bmatrix} m_{00}^{i} \pm \left(\sqrt{m_{00}^{i}}/g\right) \\ m_{01}^{i} \pm \left(\sqrt{m_{01}^{i}}/g\right) \\ m_{02}^{i} \pm \left(\sqrt{m_{02}^{i}}/g\right) \end{bmatrix}, \tag{18}$$

where g is the detector gain. The error associated with the demodulation matrix is then evaluated starting from these two additional sets of matrices following the method as per Eq. (6) in Lefebvre et al. (2000).

The mathematical model has to be applied to each one of the pixel within the detector. As a result, the analysis generates a number of modulation and demodulation matrices equal to the number of pixels. These matrices can be combined by collecting in a single two-dimensional array the values derived for the same element over all the resulting matrices. This array will have the same dimensions as the images captured by the instrument. This process generates 12 separate images, one for each element, reporting the values of that element of the modulation and demodulation matrices over the whole detector.

3.2. Calibration procedure

The Metis coronagraph calibration campaign took place at the Optical Payload System (OPSys) facility owned by the INAF and hosted by the Aerospace Logistic Engineering Company (ALTEC S.p.A.), in Turin, Italy (Fineschi et al. 2011, 2019).

To achieve the calibration campaign goal, that is to obtain the instrument demodulating schema, we used the setup shown in the schematic in Fig. 5. The Metis coronagraph was placed on the optical bench of the SPace Optics Calibration Chamber (SPOCC). An extended spatially uniform light source was placed in front of the instrument aperture, and a LP was positioned in the space between the instrument and the source. The LP, hereafter referred to as the pre-polarizer, was rotated to inject into the instrument a collimated light beam with well-known polarimetric characteristics. Before this test, the pre-polarizer was characterized to verify that its polarizing properties were uniform over its full aperture and that the exit light beam could be modeled with the theoretical Stokes vector, and hence with a negligible error.

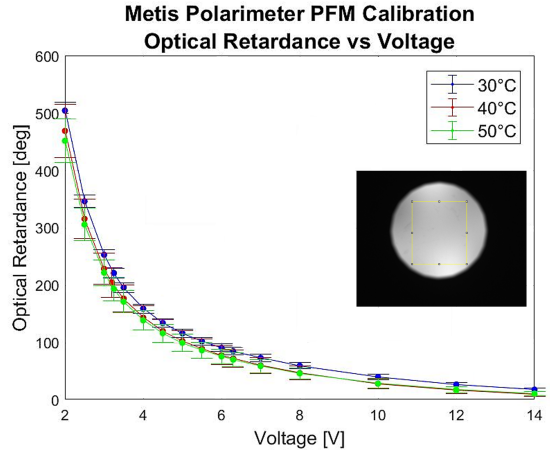

Fig. 4. Optical retardance vs. voltage curves of the Metis polarimeter obtained for three different temperatures of the LCVR cells and an example of an image acquired during the test. Each point of the curves shows the average of the value measured within the yellow rectangle shown in the example of acquired images. The error bars represent the standard deviation.

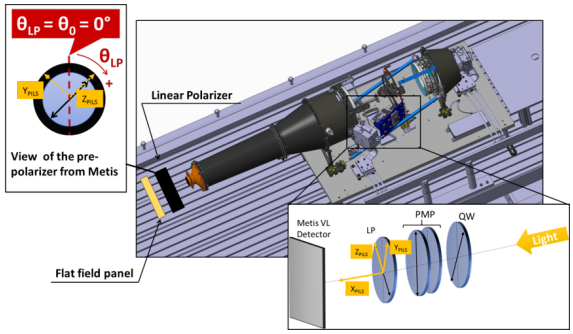

Fig. 5. Schema of the setup used to characterize the polarimetric visible-light channel of the Metis coronagraph. An extended spatially uniform light source and a LP were placed in front of the instrument to generate a uniformly polarized light beam. The frame of reference used to analyze the data is shown in the polarimeter schema, together with the axis of maximum transmittance of all the polarizing elements involved in the setup.

We acquired data with the Metis instrument for five different angular positions of the pre-polarizer maximum transmittance axis and for a set of 40 voltages applied to the LCVR cells. These voltage values were selected based on the results obtained from the characterization of the polarimeter as a subsystem and that describe the relationship between the applied voltage and the resulting angle of retardance. The interdependence of these two parameters is represented by the curve in Fig. 4, which reaches optical retardance values greater than 360°; this is a graphical choice of the authors to show the curve connecting this value to the applied voltage.

Figure 6 shows four images acquired during the Metis calibration campaign. Each of these images corresponds to a different voltage value set to the LCVR cells, providing an example of the modulating capabilities of the Metis polarimeter. Comparing the first and third images starting from the left side, it is clear how the voltage caused an angle of retardance of about 180° in the incident radiation. The last one, instead of having its associated polarization vector parallel to the axis of maximum transmittance of the LP inside the polarimeter, the so-called analyzer, has a vector perpendicular to it. As a consequence, the measured

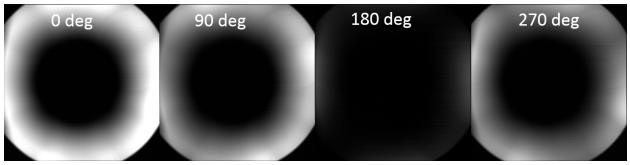

Fig. 6. Example of images acquired during the calibration campaign of the Metis coronagraph. The voltages applied to the LCVR cells provide a rotation of the incident light polarization vector of 0, 45, 90 and 180 deg, shown here from left to right.

Table 1. Voltage values and their corresponding angle of retardance for the Metis PMP.

Applied voltage [V]	Retardance [deg]
7.25	49.1
4.60	84.3
3.36	133.2
2.77	181.8 (=0)

signal is equal to its minimum value in the full image. It is worth pointing out that, since the used light source is uniform over the instrument field of view, the occulting element and its consequent vignetting effect are clearly visible in the acquired images. More details on the Metis vignetting are given in Casini et al. (2023).

3.3. Results

The first result obtained from the analysis of the acquired images is a group of 12 two-dimensional arrays. Each of these arrays collects the value of a single element of the modulation matrix derived for each pixel over the full image. This collection of arrays is fundamental to derive the final result of the analysis: a set of 12 two-dimensional arrays that allows us to interpret from a polarimetric point of view the images acquired by the Metis coronagraph and derive the Stokes vector associated with the coronal light, useful to quantify the amount of observed polarized brightness.

We obtained the following results by considering the data acquired for four angular positions of the linear pre-polarizer positioned upstream the setup: −45, 0, 45, and 90 deg. These angles are given with respect to the acceptance axis of the LP inside the polarimeter, and are evaluated in the frame of reference defined for the instrument and used for the data analysis. To be able to measure the optimal Stokes vector describing the coronal light, we decided to apply to the cell the voltages leading to a value of the efficiency vector as close as possible to the maximum one. These voltages and their associated retardance angles are reported in Table 1. As is possible to see, we selected voltage values ensuring four different angles separated by about 45°. The table reports the values associated with a single LCVR cell, while the Metis polarimeter contains two of them. Their total effect is given by the sum of the two angles of retardance introduced by each of the two identical cells.

Due to its optical design, we can assume in first approximation that the polarization introduced by the optics inside the Metis coronagraph represents a negligible component, so we used Eq. (12) as a mathematical model for the entire instrument in the described analysis.

Table 2. Summary of the analysis for the modulation tensor.

Element	Target value	Exp. value	Median	Std
x_{00}	0.50	0.50	0.51	0.13
x_{01}	0.50	0.50	0.39	0.23
x_{02}	0.00	0.03	0.00	0.20
x_{10}	0.50	0.50	0.49	0.12
x_{11}	0.00	−0.07	−0.04	0.18
x_{12}	0.50	0.50	0.36	0.21
x_{20}	0.50	0.50	0.49	0.12
x_{21}	−0.50	−0.49	−0.38	0.19
x_{22}	0.00	0.09	0.03	0.20
x_{30}	0.50	0.50	0.50	0.12
x_{31}	0.00	−0.03	0.03	0.20
x_{32}	−0.50	−0.49	−0.38	0.21

Equation (19) reports the theoretical modulation matrix associated with the Metis coronagraph when the retardance values shown in Table 1 are considered:

$$X_{\mathrm{Metis}} = \frac{1}{2}\begin{bmatrix} 1.00 & 1.00 & 0.06 \\ 1.00 & -0.14 & 0.99 \\ 1.00 & -0.98 & 0.19 \\ 1.00 & -0.06 & -0.99 \end{bmatrix}. \tag{19}$$

The theoretical demodulation matrix for each pixel can be derived by calculating the pseudo-inverse of the matrix in Eq. (19), which is close to the percent to the one shown in Eq. (16) and associated with the maximum efficiency value:

$$X^{\dagger}_{\mathrm{Metis}} = \frac{1}{2}\begin{bmatrix} 1.08 & 0.88 & 0.91 & 1.12 \\ 2.13 & -0.01 & -1.88 & -0.24 \\ 0.20 & 1.87 & 0.07 & -2.14 \end{bmatrix}. \tag{20}$$

Equations (19) and (20) can be used as a reference in the interpretation of the results obtained deriving the modulation and demodulation matrices for all pixels in the images. The average of the elements contained in the derived two-dimensional array should be close to the correspondent element in these two equations.

Before solving the system of equations shown in Eq. (12), we normalized the acquired measurements by dividing the images by the measured total brightness:

$$\overline{I^{(n)}} = \frac{I^{(n)}}{\frac{1}{2}\sum_{k=1}^{4} I^{(k)}}. \tag{21}$$

Figure 7 shows the 12 two-dimensional arrays that collect the values derived for each pixel of the instrument for a single element of the modulation matrix. The white circular area in the plots corresponds to the position of the occulting element; due to its presence, the light cannot reach that region of the detector, so it is not possible to analyze the modulation performed by the polarimeter.

Table 2 reports a summary of the values shown in Fig. 7. For each array, the table lists the target value (see Eq. (15)), the expected value according to the applied voltage as shown in Eq. (19), and the median and standard deviation values of the distribution of that element over all pixels.

To derive the set of arrays that collect the elements of the demodulation matrix, we inverted the modulation matrix obtained for each pixel and reorganized the results into 12 images. Fig. 8 shows the 12 resulting arrays.

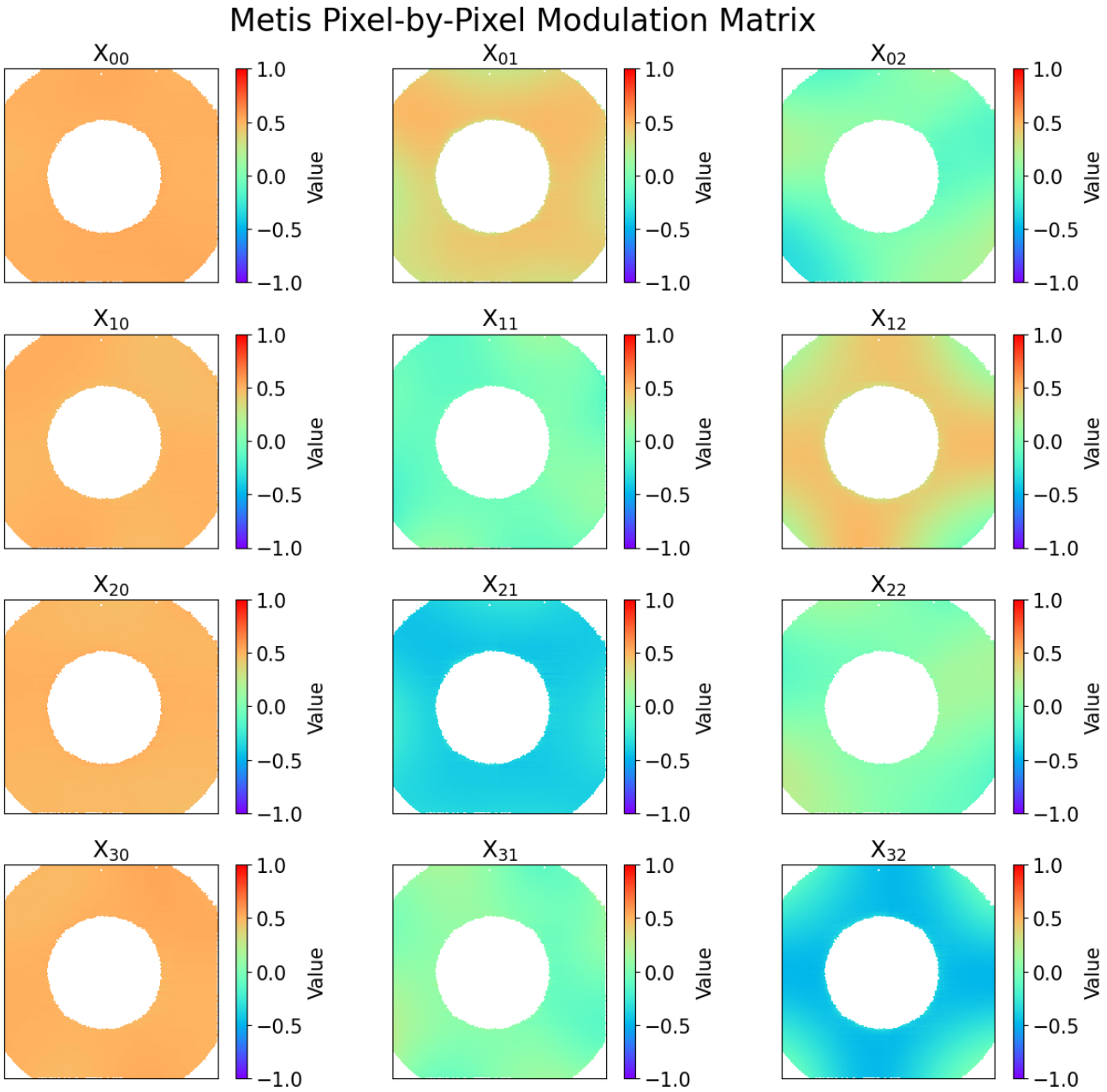

Fig. 7. Modulation tensor obtained from the Metis polarized visible channel calibration. Each image shows the value derived for each pixel for the respective element of its modulation matrix.

Table 3 reports a summary of the analysis results. For each element of the demodulation matrices, the table lists the target value (see Eq. (16)), the expected value according to the applied voltage as shown in Eq. (20), and the median and the standard deviation values of the distribution of that element over all pixels.

Figure 7 highlights two main characteristics. The images that gather the elements within the first column of the modulation matrix of each pixels look uniform. The median of the distribution is close to the expected value, and the standard deviation associated with these images is the smallest one in Table 2. This is a direct consequence of the use of normalized measurements as input to the mathematical model. This was done with the purpose of obtaining values within the range −1 to +1, which is more intuitive for a fast check with the theoretical modulation matrix. The second characteristic is the visible nonuniformity over the field of view obtained in the results for the other arrays. In this case, the difference between the median of their distributions and the theoretical value is larger, as well as the standard deviation, indicating a larger variability in the results. As can be observed in Fig. 7, the pixels positioned at the edge of the field of view and in the direction of the image diagonals lead to a value different from the theoretical one, and this behavior is clearly visible in elements such as X_{12} and X_{32}. These two characteristics are inherited by the arrays showing the demodulation matrix elements, as visible in Fig. 8, where the elements of the first row are uniform and close to the mean value, while the other images show a larger distribution of values and, consequently, a larger standard deviation. There are several reasons for this behavior. Looking at the LCVR cells, different portions

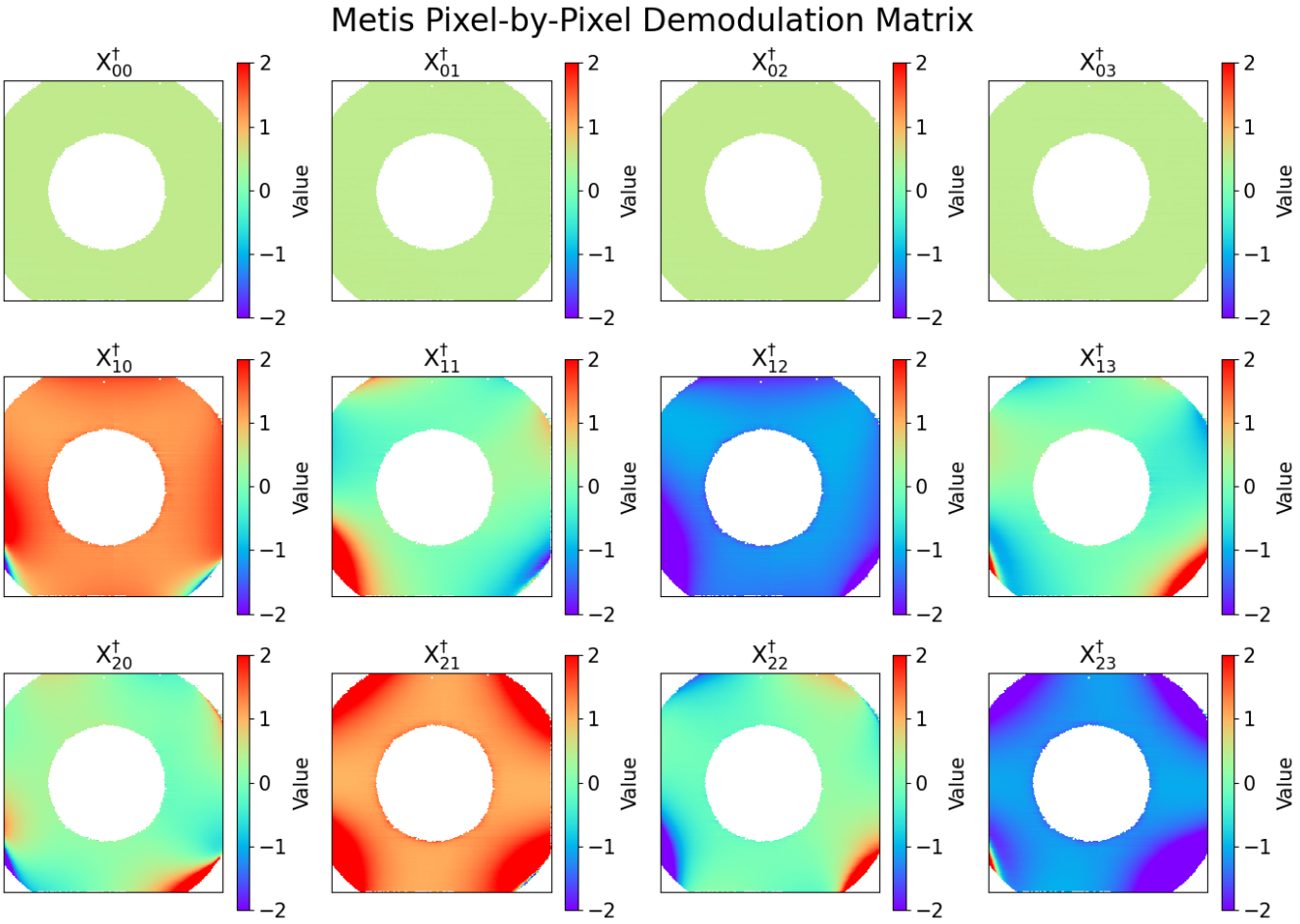

Fig. 8. Demodulation tensor obtained from the Metis polarized visible channel calibration. Each image shows the value derived for each pixel for the respective element of its demodulation matrix.

Table 3. Summary of the analysis for the demodulation tensor.

Element	Target value	Exp. value	Median	Std
$x^{\dagger}_{00}$	0.5	0.54	0.50	0.07
$x^{\dagger}_{01}$	0.5	0.44	0.50	0.08
$x^{\dagger}_{02}$	0.5	0.45	0.50	0.06
$x^{\dagger}_{04}$	0.5	0.56	0.50	0.07
$x^{\dagger}_{10}$	1.00	1.06	1.21	4.47
$x^{\dagger}_{11}$	0.00	0.00	0.00	4.79
$x^{\dagger}_{12}$	−1.00	−0.94	−1.22	4.23
$x^{\dagger}_{13}$	0.00	−0.12	−0.07	5.76
$x^{\dagger}_{20}$	0.00	0.10	0.14	9.23
$x^{\dagger}_{21}$	1.00	0.93	1.17	4.39
$x^{\dagger}_{22}$	0.00	0.03	−0.05	5.58
$x^{\dagger}_{23}$	−1.00	−1.12	−1.22	7.96

of the light beam cross the cells in a different area of their clear aperture, encountering different molecules of crystals that might react to the electric field in a slightly different way. The design of the LCVR cells is optimized to achieve the peak performance within the central area. Despite the wider field of view achieved due to the use of two LCVR cells instead of one, the outer portion of the field of view still suffers in polarization efficiency; its value is lower than the one measured in the central portion of the instrument field of view. Moreover, as a result of the assembly process, we expect the molecules close to the external diameter of the cells to be clamped, and hence limited in their range of possible angular rotation. This would result in a limit to their modulation capabilities. When we consider the LCVR cells as part of the Metis coronagraph, we also need to take into account that the central part of the instrument is occulted and that the observed scene is vignetted. Fig. 6 shows that the same areas where the values of the demodulation matrix are farther away from the expected ones are more vignetted, and this is more visible in the images acquired at 90 and 270°. We want to point out that the goal of this analysis is to derive a method of measuring the Stokes vector of the incoming radiation, and that takes into account and corrects for all these different factors that cause nonuniformity in the acquired images. The distribution of values within the resulting matrices shows how these effects are compensated for.

The efficiency vector is calculated by means of Eq. (13), using the median of the value distributions reported in Table 3, from which we obtain

$$\epsilon = (1.00, 0.58, 0.59)\,. \tag{22}$$

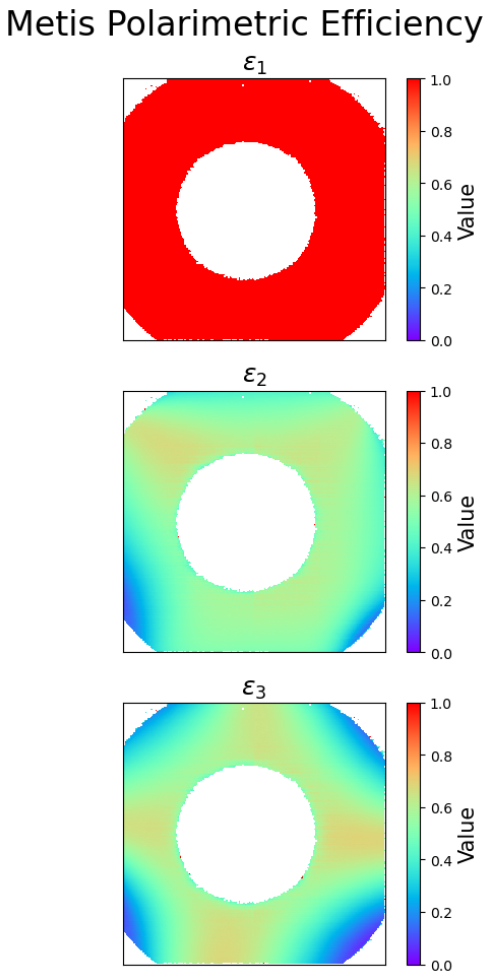

Fig. 9. Polarimetric efficiency of the demodulation schema. The maximum theoretical efficiency, calculated as per Eq. (17), is reached in the central portions of the field of view. The efficiency are lower in the outer areas due to the clamped edges of the LCVR cells.

The efficiency values are lower than expected when compared to Eq. (17). However, those values are the averages of the pixel by pixel efficiencies that have a large variability, as shown in Fig. 9. There it is possible to see how the distribution of values changes within the images, reaching the maximum closer to the central area.

The successful application of the demodulation tensor obtained from the calibration of the Metis coronagraph on-ground has been reported by Liberatore et al. (2023), where the average value of the polarized brightness is reported for the whole intensity obtained from data acquired during a roll maneuver. This has been evaluated with both the theoretical and measured demodulation tensor (Figs. 10 and 11 in Liberatore et al. 2023), and the authors show that when using the latter, the variation in the measured polarized brightness stays within the error. This is due to the fact that the measured demodulation tensor accounts for the deviation of the polarization state of the incident light due to disuniformity in the material or to instrumental polarization.

4. Conclusions

This work describes the calibration of the polarimetric visible-light channel of the Metis coronagraph. Metis measures the polarization state of the incident polarized light thanks to a polarimeter, which is equipped with two LCVR cells that represent the modulating element of the instrument. By applying a voltage to the cells, it is possible to rotate the polarization orientation of the observed light by a certain angle, depending on the level of applied voltage.

The goal of the polarimetric characterization of the Metis coronagraph was to derive a means of measuring the polarized brightness of the observed coronal light. This was achieved in several steps. First, we characterized the polarimeter before its integration in the instrument to derive the relationship between the applied voltage and the consequent angle of retardance introduced in the incident polarized light beam. Once this relation was known and the instrument integration was completed, we chose a set of four voltages to modulate the light during the instrument calibration activities. The collected dataset allowed us to derive first the modulation and then the demodulation matrix associated with each pixel within the detector. These matrices link the measured intensity to the vector that describes the polarization state of the observed light.

The result is a set of 12 two-dimensional arrays that allows us to measure the Stokes vector of the observed K-corona light and, consequently, quantify the coronal electron density.

As final remark, the arrays collecting the demodulation matrix elements derived for each pixel deviate from the expected values; this is due to the intrinsic nonuniformity of the system, which is related to how the molecules are integrated inside the cells, and to the interaction of the light with the other optical elements within the Metis coronagraph. Since the mathematical model used in the analysis is meant to compensate for these effects, this result was expected. This is more visible in the derived polarimetric efficiency, which is closer to the theoretical maximum value in the central part of the field of view, where we would expect the instrument to perform better than at the edges of the image.

Acknowledgements. Solar Orbiter is a space mission of international collaboration between ESA and NASA, operated by ESA. The Metis programme is supported by the Italian Space Agency (ASI) under the contracts to the co-financing National Institute of Astrophysics (INAF): Accordi ASI-INAF N. I-043-10-0 and Addendum N. I-013-12-0/1, Accordo ASI-INAF N.2018-30-HH.0 and under the contracts to the industrial partners OHB Italia SpA, Thales Alenia Space Italia SpA and ALTEC: ASI-TASI N. I-037-11-0 and ASI-ATI N. 2013-057-I.0. Metis was built with hardware contributions from Germany (Bundesministerium für Wirtschaft und Energie (BMWi) through the Deutsches Zentrum für Luft- und Raumfahrt e.V. (DLR)), from the Academy of Sciences of the Czech Republic (Czech PRODEX) and from ESA.

References

Alvarez-Herrero, A., Uribe-Patarroyo, N., García Parejo, P., et al. 2011, SPIE Conf. Ser., 8160, 81600Y
Álvarez Herrero, A., Parejo, P. G., Laguna, H., et al. 2015, Proc. SPIE, 9613, 96130I
Alvarez-Herrero, A., García Parejo, P., Laguna, H., et al. 2017, SPIE Conf. Ser., 10563, 105632Z
Alvarez-Herrero, A., García Parejo, P., Campos-Jara, A., et al. 2024, SPIE Conf. Ser., 13050, 130500H
Antonucci, E., Dodero, M. A., & Giordano, S. 2000, Sol. Phys., 197, 115
Antonucci, E., Fineschi, S., Naletto, G., et al. 2012, Proc. SPIE, 8443, 844309
Antonucci, E., Romoli, M., Andretta, V., et al. 2020, A&A, 642, A10
Antonucci, E., Downs, C., Capuano, G. E., et al. 2023, Phys. Plasmas, 30, 022905
Bass, M. 1995, Handbook of Optics (New York: McGraw Hill Inc.), 2
Berghmans, D., Auchère, F., Long, D. M., et al. 2021, A&A, 656, L4
Billings, D. E. 1966, A Guide to the Solar Corona (New York: Academic Press)
Capitani, C., Cavallini, F., Ceppatelli, G., et al. 1989, Sol. Phys., 120, 173
Capobianco, G., Casti, M., Fineschi, S., et al. 2018, Proc. SPIE, 10698, 1069830
Casini, C., Chioetto, P., De leo, Y., et al. 2023, SPIE Conf. Ser., 12777, 1277705
Chipman, R. A. 1988, Proc. SPIE, 891, 10

Chipman, R. A. 1990, Proc. SPIE, 1166, 79
Collett, E. 1992, Polarized Light. Fundamentals and Applications (New York: Dekker)
Collett, E. 2005, Field Guide to Polarization (SPIE)
Cranmer, S. R. 2020, ApJ, 900, 105
Cranmer, S. R., Kohl, J. L., Noci, G., et al. 1999, ApJ, 511, 481
Crescenzio, G., Fineschi, S., Capobianco, G., et al. 2012, Proc. SPIE, 8443, 84433J
De Senarmont, H. 1840, Ann. Chim. Phys., 73, 337
del Toro Iniesta, J. C., & Collados, M. 2000, Appl. Opt., 39, 1637
Domingo, V., Fleck, B., & Poland, A. I. 1995, Sol. Phys., 162, 1
Fineschi, S., Antonucci, E., Romoli, M., et al. 2003, Proc. SPIE, 4853, 162
Fineschi, S., Zangrilli, L., Rossi, G., et al. 2005, Proc. SPIE, 5901, 389
Fineschi, S., Crescenzio, G., Massone, G., et al. 2011, Proc. SPIE, 8148, 81480W
Fineschi, S., Antonucci, E., Romoli, M., et al. 2013, Proc. SPIE, 8862, 88620G
Fineschi, S., Casti, M., Capobianco, G., et al. 2019, 2019 IEEE 5th International Workshop on Metrology for AeroSpace (MetroAeroSpace) (IEEE), 309
Fineschi, S., Naletto, G., Romoli, M., et al. 2020, Exp. Astron., 49, 239
García Parejo, P., & Álvarez-Herrero, A. 2019, Opt. Mater. Express, 9, 2681
Heredero, R. L., Uribe-Patarroyo, N., Belenguer, T., et al. 2007, Appl. Opt., 46, 689
Hyder, C. L., & Lites, B. W. 1970, Sol. Phys., 14, 147
Kohl, J. L., Esser, R., Gardner, L. D., et al. 1995, Sol. Phys., 162, 313
Kohl, J. L., Noci, G., Antonucci, E., et al. 1997, Sol. Phys., 175, 613
Koutchmy, S., & Lamy, P. 1984, Proc. 85th Colloq. Int. Astron. Union, 85, 141
Koutchmy, S., & Lamy, P. L. 1985, Int. Astron. Union Colloq., 85, 63
Lamy, P., Llebaria, A., Boclet, B., et al. 2020, Sol. Phys., 295, 89
Lamy, P., Gilardy, H., Llebaria, A., Quémerais, E., & Ernandez, F. 2021, Sol. Phys., 296, 76
Landini, F., Romoli, M., Fineschi, S., & Antonucci, E. 2006, Appl. Opt., 45, 6657
Lefebvre, M., Keeler, R. K., Sobie, R., & White, J. 2000, Nucl. Instrum. Meth. Phys. Res. A, 451, 520
Liberatore, A., Fineschi, S., Casti, M., et al. 2023, A&A, 672, A14
Mann, I. 1992, A&A, 261, 329
Marsch, E., Antonucci, E., Bochsler, P., et al. 2000, Solar Orbiter, Assessment Study Report 6 (ESA-SCI)
McGuire, J. P., & Chipman, R. A. 1994, Appl. Opt., 33, 5080
Minnaert, M. 1930, Z. Astrophys., 1, 209
Moses, J. D., Antonucci, E., Newmark, J., et al. 2020, Nat. Astron., 4, 1134
Müller, D., St. Cyr, O. C., Zouganelis, I., et al. 2020, A&A, 642, A1
Naletto, G., Antonucci, E., Andretta, V., et al. 2010, Proc. ICSO, 10565, 105656H
Parejo, P. G., Álvarez-Herrero, A., Capobianco, G., & Fineschi, S. 2019, J. Astron. Telesc. Instrum. Syst., 5, 034002
Ramos, A. A., & Collados, M. 2008, Appl. Opt., 47, 2541
Romoli, M., Antonucci, E., Andretta, V., et al. 2021, A&A, 656, A32
Saleh, B. E., & Teich, M. C. 1991, Fundamentals of Photonics (New York: John Wiley and Sons)
Silva-López, M., Bastide, L., Restrepo, R., et al. 2017, Sensor Actuators, 266, 247
Skumanich, A., Lites, B. W., Pillet, V. M., & Seagraves, P. 1997, ApJS, 110, 357
Snik, F., Craven-Jones, J., Escuti, M., et al. 2014, SPIE Conf. Ser., 9099, 90990B
Telloni, D., Zank, G. P., Stangalini, M., et al. 2022, ApJ, 936, L25
Telloni, D., Antonucci, E., Adhikari, L., et al. 2023, A&A, 670, L18
Tyo, J. S., Goldstein, D. L., Chenault, D. B., & Shaw, J. A. 2006, Appl. Opt., 45, 5453
Uribe-Patarroyo, N., Alvarez-Herrero, A., García Parejo, P., et al. 2011, SPIE Conf. Ser., 8148, 814810
Van de Hulst, H. 1950, Bull. Astron. Inst. Netherlands, 11, 135
Withbroe, G. L., Kohl, J. L., Weiser, H., & Munro, R. H. 1982, Space Sci. Rev., 33, 17